V International Conference on Computational Methods for Coupled Problems in Science and Engineering
COUPLED PROBLEMS 2013
S. Idelsohn, M. Papadrakakis and B. Schrefler (Eds)

THERMOCHEMICAL HEAT STORAGE FOR SUSTAINABLE POWER GENERATION – MODEL DEVELOPMENT BASED ON THE THEORY OF POROUS MEDIA AND NUMERICAL IMPLEMENTATION

THOMAS NAGEL[†,*], HAIBING SHAO[†], ASHOK K. SINGH[†], NORIHIRO WATANABE[†], MARC LINDER[◇], ANTJE WÖRNER[◇] AND OLAF KOLDITZ[†,‡]

[†]Department of Environmental Informatics, Helmholtz Centre for Environmental Research – UFZ,
Permoserstr. 15, 04318 Leipzig, Germany
Email: thomas.nagel@ufz.de

[◇]Institute of Technical Thermodynamics, German Aerospace Center (DLR e.V.),
Pfaffenwaldring 38-40, 70569 Stuttgart, Germany

[‡]Applied Environmental Systems Analysis, Dresden University of Technology, Germany

Key words: Thermochemical heat storage, porous media, reactive transport, thermal non-equilibrium, finite element

Abstract.

1 INTRODUCTION

The competitiveness of renewable energy sources for heat generation and the efficient use of industrial process heat require the integration of reliable thermal energy storage systems. Aside from sensible and latent heat storage concepts thermochemical heat storage systems are an attractive option due to their high storage densities and low losses [8]. Their development is still at a laboratory stage and can be greatly supported by advanced theoretical and numerical models that facilitate process understanding and optimisation [11]. Here we present a model based on the Theory of Porous Media and the assumption of local thermal non-equilibrium for a solid reactor with a direct heat transfer gas carrying a gaseous reactant. Appropriate kinematic and balance relations are established to account for mass and heat transport as well as phase and mass transfer due to exo- and endothermic chemical reactions. They are supplemented by constitutive relations that are derived from and constrained by the Clausius-Duhem inequality in a thermodynamically consistent manner. The highly nonlinear governing equations are cast into the weak form and discretised in space following a standard Galerkin approach and in time using a generalized single-step algorithm. The model has been implemented into the scientific open source finite element code OpenGeoSys designed for strongly coupled THMC processes [7]. A calcium oxide / calcium hydroxide reaction system through which a nitrogen-steam gas

mixture passes is taken as a model system. The simulations show a fast and a slow reaction wave travelling through the reactor that are limited by system equilibrium temperature / heat transport and the degree of conversion of the solid material, respectively. It is shown how the system performance, e.g. in terms of outlet heat profiles, can be adapted to specific needs by varying process and material parameters.

2 METHODS

2.1 General balance equations

The model development was based on the well established Theory of Porous Media (TPM) [5, 3]. Without additional derivation the general local balance relations employed here will be listed in this section. The balance of mass for a phase α subject to mass exchange with other phases is

$$\frac{\mathrm{d}_\alpha \rho_\alpha}{\mathrm{d}t} + \rho_\alpha \mathrm{div}\, \boldsymbol{v}_\alpha = \hat{\rho}_\alpha \quad \text{with} \quad \sum_\alpha \hat{\rho}_\alpha = 0 \tag{1}$$

where $(\bullet)'_\alpha = \frac{\mathrm{d}_\alpha(\bullet)}{\mathrm{d}t} = \frac{\partial(\bullet)}{\partial t} + \mathrm{grad}\,(\bullet)\cdot\boldsymbol{v}_\alpha$ denotes a material time derivative following the motion of the α^{th} constituent (velocity $\boldsymbol{v}_\alpha$, apparent density ρ_α). The symbol $\hat{(\bullet)}$ denotes production terms due to internal interactions.

The quasistatic balance of linear momentum in the absence of body forces reads

$$\mathrm{div}\, \boldsymbol{\sigma}_\alpha + \hat{\boldsymbol{s}}_\alpha = \hat{\rho}_\alpha \boldsymbol{v}_\alpha \quad \text{with} \quad \sum_\alpha \hat{\boldsymbol{s}}_\alpha = \sum_\alpha (\hat{\boldsymbol{p}}_\alpha + \hat{\rho}_\alpha \boldsymbol{v}_\alpha) = \boldsymbol{0} \tag{2}$$

with the partial Cauchy stress tensor $\boldsymbol{\sigma}_\alpha$, the overall and direct momentum production terms $\hat{\boldsymbol{s}}_\alpha$ and $\hat{\boldsymbol{p}}_\alpha$, respectively.

Due to the presence of mass exchange the first law of thermodynamics was expressed in terms of enthalpy rather than inner energy. For that purpose, the Cauchy stress and rate of deformation tensors were split into deviatoric and hydrostatic parts [10]

$$\boldsymbol{\sigma}_\alpha = \boldsymbol{\sigma}^D_\alpha - p_\alpha \boldsymbol{I} \quad \text{with} \quad p_\alpha = -\frac{1}{3}(\boldsymbol{\sigma}_\alpha : \boldsymbol{I}) \tag{3}$$

$$\boldsymbol{d}_\alpha = \boldsymbol{d}^D_\alpha + \frac{1}{3}(\boldsymbol{d}_\alpha : \boldsymbol{I})\boldsymbol{I} \tag{4}$$

The enthalpy balance (with h_α the specific enthalpy and $\boldsymbol{q}_\alpha$ as the partial heat flux vector)

$$\rho_\alpha (h_\alpha)'_\alpha - (p_\alpha)'_\alpha - \boldsymbol{\sigma}^D_\alpha : \boldsymbol{d}^D_\alpha - \rho_\alpha r_\alpha + \mathrm{div}\, \boldsymbol{q}_\alpha = \hat{u}_\alpha - \hat{\rho}_\alpha \left(h_\alpha + \frac{1}{2}\boldsymbol{v}_\alpha \cdot \boldsymbol{v}_\alpha \right) - \boldsymbol{v}_\alpha \cdot \hat{\boldsymbol{p}}_\alpha \tag{5}$$

is subject to a constraint on the inner energy production terms

$$\sum_\alpha \hat{u}_\alpha = 0 \tag{6}$$

Constitutive relations are required to close the above system of equations. The Clausius-Duhem inequality was used in the form

$$\sum_{\alpha} \frac{1}{T_\alpha} \left[-\rho_\alpha [(\psi_\alpha)'_\alpha + (T_\alpha)'_\alpha \eta_\alpha] - \hat{\rho}_\alpha \left(\psi_\alpha + \frac{p_\alpha}{\rho_\alpha} + \frac{1}{2} \boldsymbol{v}_\alpha \cdot \boldsymbol{v}_\alpha \right) + \boldsymbol{\sigma}^D_\alpha : \boldsymbol{l}^D_\alpha + \right.$$
$$\left. + p_\alpha \frac{(\phi_\alpha)'_\alpha}{\phi_\alpha} + p_\alpha \frac{(\rho_{\alpha R})'_\alpha}{\rho_{\alpha R}} - \hat{\boldsymbol{p}}_\alpha \cdot \boldsymbol{v}_\alpha - \frac{1}{T_\alpha} \boldsymbol{q}_\alpha \cdot \operatorname{grad} T_\alpha + \hat{u}_\alpha \right] \geq 0 \tag{7}$$

to ensure the thermodynamic consistency of the relations used in this study. Here, T_α is the absolute temperature, ψ_α the specific Helmholtz free energy, η_α the specific entropy, ϕ_α the volume fraction and $\rho_{\alpha R} = \rho_\alpha / \phi_\alpha$ the real density of phase α. Specifically, a porous solid skeleton saturated by a gas was considered here. The saturation constraint

$$0 = \sum_{\alpha = S,G} (\phi_\alpha)'_\alpha - \operatorname{grad} \phi_G \cdot (\boldsymbol{v}_G - \boldsymbol{v}_S) \tag{8}$$

was multiplied with a Lagrange multiplier and the inverse reference temperature [4]

$$\frac{1}{T_R} = \frac{1}{2} \frac{T_S + T_G}{T_S T_G} \tag{9}$$

and added to the entropy inequality. Additionally, the gas was considered a mixture of ideal gases (components ζ) with $\phi_G = \phi_\zeta$ and $T_G = T_\zeta$ [6]. The final version of the entropy inequality thus reads

$$\begin{aligned} 0 \leq & \frac{1}{T_S} \left[-\rho_S [(\psi_S)'_S + (T_S)'_S \eta_S] - \hat{\rho}_S \left(\psi_S + \frac{p_S}{\rho_S} + \frac{1}{2} \boldsymbol{v}_S \cdot \boldsymbol{v}_S \right) + \boldsymbol{\sigma}^D_S : \boldsymbol{l}^D_S + \right. \\ & \left. + p_S \frac{(\phi_S)'_S}{\phi_S} + p_S \frac{(\rho_{SR})'_S}{\rho_{SR}} - \hat{\boldsymbol{p}}_S \cdot \boldsymbol{v}_S - \frac{1}{T_S} \boldsymbol{q}_S \cdot \operatorname{grad} T_S + \hat{u}_S \right] + \\ & + \frac{1}{T_G} \sum_{\zeta} \left[-\rho_\zeta [(\psi_\zeta)'_\zeta + (T_G)'_\zeta \eta_\zeta] - \hat{\rho}_\zeta \left(\psi_\zeta + \frac{p_\zeta}{\rho_\zeta} + \frac{1}{2} \boldsymbol{v}_\zeta \cdot \boldsymbol{v}_\zeta \right) + \boldsymbol{\sigma}^D_\zeta : \boldsymbol{l}^D_\zeta + \right. \\ & \left. + p_\zeta \frac{(\phi_G)'_G}{\phi_G} + \frac{p_\zeta}{\phi_G} \operatorname{grad} \phi_G \boldsymbol{d}_\zeta + p_\zeta \frac{(\rho_{\zeta R})'_\zeta}{\rho_{\zeta R}} - \hat{\boldsymbol{p}}_\zeta \cdot \boldsymbol{v}_\zeta - \frac{1}{T_G} \boldsymbol{q}_\zeta \cdot \operatorname{grad} T_G + \hat{u}_\zeta \right] + \\ & + \frac{1}{T_R} \lambda \left[(\phi_S)'_S + (\phi_G)'_G - \operatorname{grad} \phi_G \cdot \boldsymbol{w}_G \right] \end{aligned} \tag{10}$$

where the seepage velocity $\boldsymbol{w}_G = \boldsymbol{v}_G - \boldsymbol{v}_S$ of the gas relative to the solid and the diffusion velocity $\boldsymbol{d}_\zeta = \boldsymbol{v}_\zeta - \boldsymbol{v}_G$ of a gas constituent in the overall gas phase have been introduced. Further details as well as the evaluation of the above relation can be found in [9].

2.2 Governing equations

The general model above was specified under the following assumptions: Local thermal non-equilibrium albeit with small deviations from equilibrium; binary gas mixture of nitrogen and

steam; rigid solid skeleton; constant porosity; Fourier's law for heat conduction. The solid gas reaction

$$\mathrm{CaO\,(s) + H_2O\,(g) \rightleftharpoons Ca(OH)_2\,(s)}$$

was taken as an example system.
The solid mass balance simply reads

$$(1-\phi_G)\frac{\partial \rho_{SR}}{\partial t} = \hat{\rho}_S \tag{11}$$

The reaction kinetics used to determine $\hat{\rho}_S$ were dependent on the degree of conversion from calcium oxide to calcium hydroxide as well as the equilibrium drop that was calculated from the Clausius-Clapeyron relation for this particular reaction:

$$\hat{\rho}_S = -(1-\phi_G) x_{mV} (\rho_{\mathrm{Ca(OH)_2}\,R} - \rho_{SR}) k_R^H \frac{T_S - T_{\mathrm{eq}}}{T_{\mathrm{eq}}} \tag{12}$$

where k_R^H is a rate constant and T_{eq} the equilibrium temperature.
The gas mass balance is found as

$$\phi_G \frac{\partial \rho_{GR}}{\partial t} + \mathrm{div}\,(\phi_G \rho_{GR} \boldsymbol{v}_G) = -\hat{\rho}_S \tag{13}$$

Under certain linearity assumptions for the momentum production terms [9, 6] the linear momentum balance of the gas yields the extended Darcy-like expression for the filter velocity $\tilde{\boldsymbol{w}}_G$ (neglecting diffusion-reaction contributions)

$$\tilde{\boldsymbol{w}}_G = -\frac{\boldsymbol{k}_S}{\mu_V}\left[\frac{p}{\phi_G}\left(1 - \frac{T_S}{T_G}\right)\mathrm{grad}\,\phi_G + \mathrm{grad}\,p\right] \tag{14}$$

with the viscosity μ_V and the intrinsic permeability tensor $\boldsymbol{k}_S$.
The heat transport equation for the gas reads

$$\begin{aligned}\phi_G \rho_{GR} c_{pG} \frac{\partial T_G}{\partial t} + \phi_G \rho_{GR} c_{pG}\,\mathrm{grad}\,T_G \cdot \boldsymbol{v}_G = h_{SG}(T_S - T_G) + \mathrm{div}\,[\phi_G \boldsymbol{\lambda}_{GR}\,\mathrm{grad}\,T_G] + \\ + \phi_G \frac{\partial p}{\partial t} + \phi_G \mathrm{grad}\,p \cdot \boldsymbol{v}_G\end{aligned} \tag{15}$$

with the specific heat capacity c_{pG}, heat conductivity $\boldsymbol{\lambda}_{GR}$ and the volumetric interphase heat transfer coefficient h_{SG}. Similarly, the heat transport equation for the solid is

$$\rho_S c_{pS} \frac{\partial T_S}{\partial t} = \mathrm{div}\,(\boldsymbol{\lambda}_S \mathrm{grad}\,T_S) + h_{SG}(T_G - T_S) - \hat{\boldsymbol{p}}_G \cdot \boldsymbol{w}_G + \hat{\rho}_S\,[\Delta h + c_{pV}(T_G - T_S)] \tag{16}$$

$$\text{with} \quad \hat{\boldsymbol{p}}_G = -\frac{\phi_G^2 \mu_V}{\boldsymbol{k}_S}\boldsymbol{w}_G + \frac{T_S}{T_G} p \mathrm{grad}\,\phi_G = \mathrm{grad}\,(\phi_G p)$$

with the specific heat capacity of the solid c_{pS} and vapour c_{pV}, heat conductivity $\boldsymbol{\lambda}_{SR}$, reaction enthalpy per unit mass Δh and seepage velocity $\boldsymbol{w}_G$. Gas properties such as c_{pG}, μ_V, ρ_{GR} etc. were modelled to depend on gas composition [2].
Finally, the mass balance for the reactive vapour component was written in terms of the vapour mass fraction x_{mV} as

$$\phi_G \rho_{GR} \frac{\partial x_{mV}}{\partial t} - \operatorname{div}\left(\rho_{GR} \boldsymbol{D} \operatorname{grad} x_{mV}\right) + \phi_G \rho_{GR} \operatorname{grad} x_{mV} \cdot \boldsymbol{v}_G = -(1 - x_{mV}) \hat{\rho}_S \tag{17}$$

Although the analysis based on Eq. (10) yielded the gradient of the mole fractions x_n as the driving force for diffusion [9, 6], the simplification used in the component mass balance is based on the assumption of a constant molar mass of the gas mixture:

$$\phi_G \boldsymbol{d}_\zeta = -x_{n\zeta}^{-1} \boldsymbol{D} \operatorname{grad} x_{n\zeta} \quad \overset{M_G = \text{const.}}{\longrightarrow} \quad \phi_G \rho_{\zeta R} \boldsymbol{d}_\zeta = -\rho_{GR} \boldsymbol{D} \operatorname{grad} x_{m\zeta} \tag{18}$$

This assumption is made in the present model only in the context of diffusion as it simplifies the treatment and diffusion is of minor importance compared to other mass transport effects in the applications under study. Anywhere else the mixture molar mass is calculated depending on the component mole fractions.

2.3 Finite element implementation

The primary variables p, T_G, T_S and x_{mV} were selected. Equations (13), (15), (16) and (17) were transformed into their weak forms and discretised following a standard Galerkin approach. Fluid velocities were substituted using Eq. (14). First order shape functions were employed. The reaction rate $\hat{\rho}_S$ (see Eqs. (11) and (12)) was determined with a local ODE solver. The non-symmetric system of equations

$$\begin{pmatrix} \boldsymbol{M}_{pp} & \boldsymbol{M}_{pT} & \boldsymbol{0} & \boldsymbol{M}_{px} \\ \boldsymbol{M}_{Tp} & \boldsymbol{M}_{TT}^G & \boldsymbol{0} & \boldsymbol{0} \\ \boldsymbol{0} & \boldsymbol{0} & \boldsymbol{M}_{TT}^S & \boldsymbol{0} \\ \boldsymbol{0} & \boldsymbol{0} & \boldsymbol{0} & \boldsymbol{M}_{cc} \end{pmatrix} \begin{pmatrix} \dot{\tilde{\boldsymbol{p}}} \\ \dot{\tilde{\boldsymbol{T}}}_G \\ \dot{\tilde{\boldsymbol{T}}}_S \\ \dot{\tilde{\boldsymbol{x}}}_{mV} \end{pmatrix} + \tag{19}$$

$$+ \begin{pmatrix} \boldsymbol{L}_{pp} + \widehat{\boldsymbol{A}}_{pp} & \boldsymbol{0} & \boldsymbol{0} & \boldsymbol{0} \\ \boldsymbol{A}_{Tp}^G & \boldsymbol{C}_{TT}^G + \boldsymbol{A}_{TT}^G + \boldsymbol{L}_{TT}^G & \boldsymbol{C}_{TT}^{GS} & \boldsymbol{0} \\ \boldsymbol{0} & \boldsymbol{C}_{TT}^{SG} & \boldsymbol{C}_{TT}^S + \boldsymbol{L}_{TT}^S & \boldsymbol{0} \\ \boldsymbol{0} & \boldsymbol{0} & \boldsymbol{0} & \boldsymbol{C}_{cc} + \boldsymbol{A}_{cc} + \boldsymbol{L}_{cc} \end{pmatrix} \begin{pmatrix} \tilde{\boldsymbol{p}} \\ \tilde{\boldsymbol{T}}_G \\ \tilde{\boldsymbol{T}}_S \\ \tilde{\boldsymbol{x}}_{mV} \end{pmatrix} = \begin{pmatrix} \boldsymbol{f}_p \\ \boldsymbol{f}_T^G \\ \boldsymbol{f}_T^S \\ \boldsymbol{f}_c \end{pmatrix}$$

was discretised in time with a generalised time stepping scheme using the impliciteness parameter θ

$$\dot{y} = \frac{y^{m+1} - y^m}{\Delta t} \quad \text{and} \quad y = \theta y^{m+1} + (1 - \theta) y^m \tag{20}$$

Detailed formulations of the element matrices and right hand side vectors used above as well as fundamental model verification can be found in [9]. Picard iterations were used to resolve further nonlinearities and the strongly coupled system of equations was solved monolithically for reasons of robustness.

2.4 Performed simulations

A one dimensional reactor model was set up. Dimensions and boundary conditions for the discharge process are listed in table 1 and material parameters can be found in table 2. Initial conditions were: $p_G(x, t = 0) = 2\,\text{bar}$, $T_G(x, t = 0) = T_S(x, t = 0) = 300\,^\circ\text{C}$, $x_{mV}(x, t = 0) = 0$. According to [11, 1] the effective volumetric heat transfer coefficient was

Table 1: Geometry and boundary conditions for the discharge of the DLR reactor.

Geometry	Boundary	Eq. (13)	Eq. (15)	Eq. (16)	Eq. (17)
$l = 0.08\,\text{m}$	$x = 0:$	$\rho_G w_n = 0.212\,\text{g/s}$	$T_G = 300\,^\circ\text{C}$	$q_n = 0$	$x_{mV} = 0.36$
$d = 0.055\,\text{m}$	$x = l:$	$p = 2\,\text{bar}$	$q_n = 0$	$q_n = 0$	$d_n = 0$

determined based on a surface heat transfer coefficient h, the porosity ϕ_G, the particle diameter d_p of the solid grains and the solid thermal conductivity λ_S:

$$h_{SG} = \frac{6(1-\phi_G)}{d_p}\left(\frac{1}{h} + \frac{d_p}{10\lambda_S}\right)^{-1} \tag{21}$$

Table 2: Material parameters of the reference reactor.

Property	*Value*
$\rho_{\text{Ca(OH)}_2\,R}$	$2200\,\text{kg m}^{-3}$
$\rho_{\text{CaO}\,R}$	$1656\,\text{kg m}^{-3}$
c_{pS}	$1200\,\text{J kg}^{-1}\,\text{K}^{-1}$
λ_S	$0.4\,\text{W m}^{-1}\text{K}^{-1}$
h	$80\,\text{W m}^{-2}\text{K}^{-1}$
D	$9.65{\cdot}10^{-5}\,\text{m}^2\text{s}^{-1}$

The following variations were run to illustrate the effect of porosity, permeability and particle diameter:

1. $\phi_G = 0.8$, $k_S = 5.0 \cdot 10^{-12}\,\text{m}^2$, $d_p = 50\,\mu\text{m}$
2. $\phi_G = 0.9$, $k_S = 8.0 \cdot 10^{-12}\,\text{m}^2$, $d_p = 50\,\mu\text{m}$
3. $\phi_G = 0.7$, $k_S = 1.0 \cdot 10^{-12}\,\text{m}^2$, $d_p = 50\,\mu\text{m}$
4. $\phi_G = 0.8$, $k_S = 8.0 \cdot 10^{-12}\,\text{m}^2$, $d_p = 500\,\mu\text{m}$

A more detailed analysis of influential parameters and specifics of the reaction kinetics will be presented elsewhere. The numerically determined energy density values were compared to theoretical values calculated with the relation

$$e_{\text{theor}} = (1-\phi_G)\frac{\Delta H}{M_{\text{H}_2\text{O}}}(\rho_{\text{Ca(OH)}_2\,R} - \rho_{\text{CaO}\,R}) \tag{22}$$

where $\Delta H = 112\,\text{kJ/mol}$ is the heat of reaction and $M_{\text{H}_2\text{O}}$ the molar mass of water

3 RESULTS

3.1 Reference case

At the onset of the process a fast reaction wave travels through the reactor (Fig. 1a), partially converts the solid material (Fig. 1b), extracts most of the steam from the gas (Fig. 1d) and heats up the reactor to equilibrium temperature (Fig. 1c). The subsequent reaction wave is slower due to heat transport limitations and converts the remainder of calcium oxide into calcium hydroxide (Fig. 1). The developing reaction kinetics lead to a somewhat dispersed reaction front with a width of about 25 % of the reactor length.

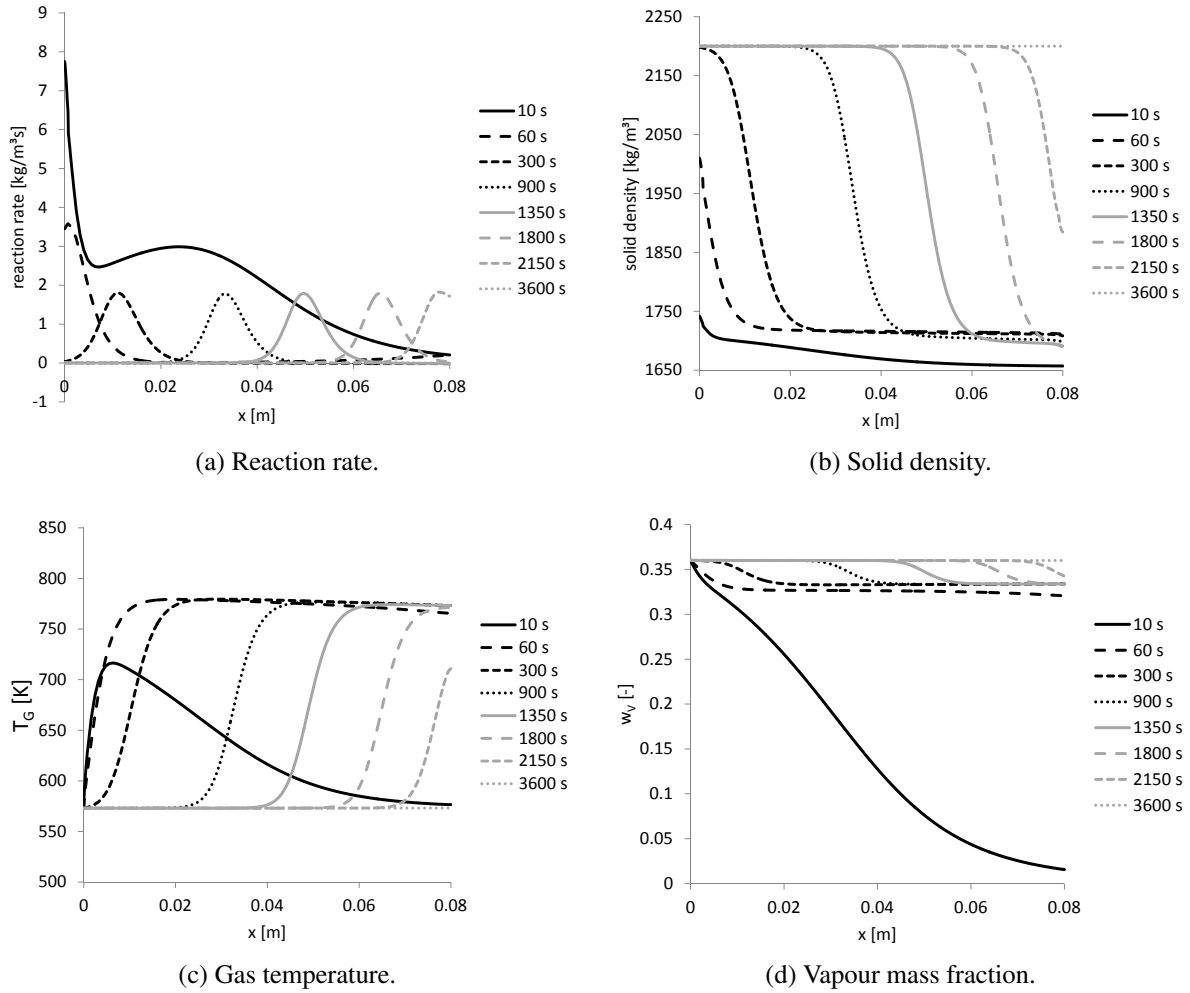

(a) Reaction rate.

(b) Solid density.

(c) Gas temperature.

(d) Vapour mass fraction.

Figure 1: Results for the reference reactor (simulation 1) plotted over the length of the reactor at various time points during the discharge.

3.2 Influence of porosity and permeability

A higher porosity translates into a lower amount of reactive solid material and thus a lower energy density (expressed here based on the reactor volume). A variation of the porosity leads to numerically predicted energy density values that correspond well to the theoretically determined ones (Fig. 2b). When plotting the gas temperature at the outlet over time it can be seen that the reactor with a porosity of 90 % is fully converted much earlier than the reactors with porosities of 80 % or 70 % (Fig. 2a). The pressure profiles in Fig. 2a exhibit the influence of the reaction on the inlet gas pressure over time and the pressure magnitudes clearly reflect the permeability variations performed in simulations 1–3. The lower permeability in the case of a porosity of 70 % causes higher pressures and thus also higher reaction equilibrium temperatures (Fig. 2a).

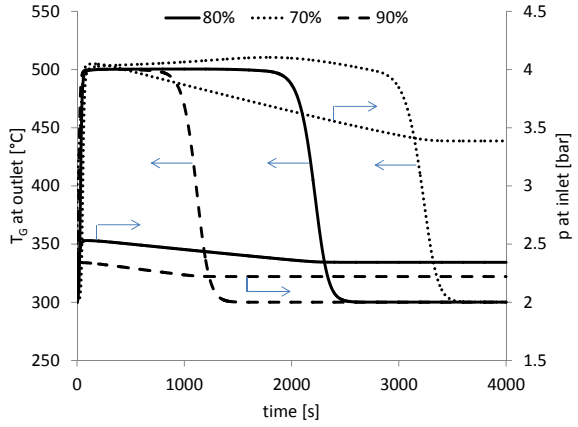

(a) Inlet pressure and outlet temperature.

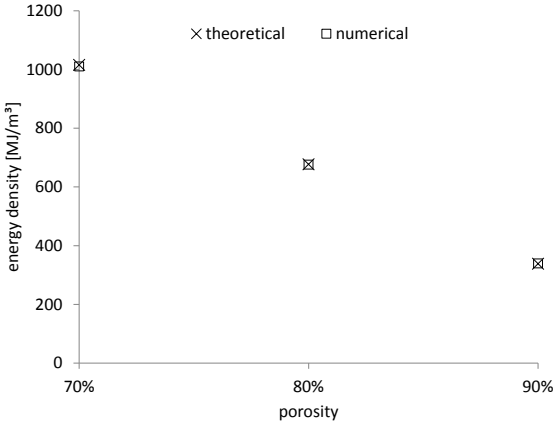

(b) Energy density.

Figure 2: Results for the porosity and permeability variations (simulations 1–3) plotted over the length of the reactor at various time points during the discharge.

3.3 Influence of particle diameter

An increase of the particle diameter from 50 µm to 500 µm causes a more pronounced local thermal non-equilibrium around the reaction front as evidenced by significantly higher gas-solid temperature differences (Fig. 3). This is due to the lower interphase heat transfer coefficient for larger particle sizes. It remains to be noted that at the inlet large temperature deviations occur also for smaller particle sizes as long as a chemical reaction is ongoing in that part of the reactor.

4 DICUSSION

A thermodynamically consistent theoretical model based on the Theory of Porous Media for reactive heat and mass transport in directly permeated thermochemical heat storage systems

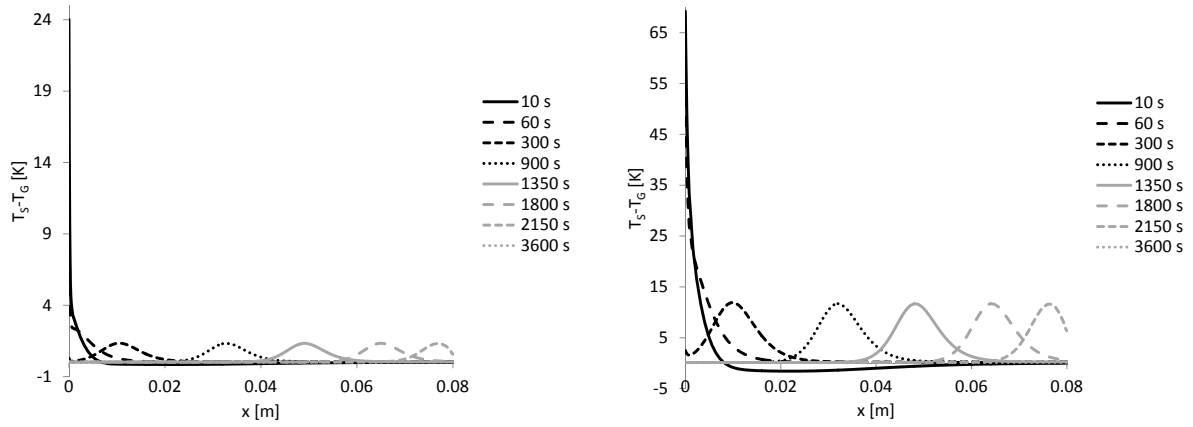

(a) $d_p = 50\,\mu\text{m}$. (b) $d_p = 500\,\mu\text{m}$.

Figure 3: Solid-gas temperature difference as an indicator of local thermal non-equilibrium for different particle diameters (simulations 1 and 4).

was developed. The numerical implementation into the finite element software OpenGeoSys was presented and applied to study an experimental reactor set-up. Parameter variations revealed the impact of the porosity on energy density and conversion time. It was shown that permeability variations do not only cause differences in local pressures but affect the temperature profiles as well. The possibility of local thermal non-equilibrium and a directly calculated local reaction rate in a manner that is coupled to other process parameters allow the model to be used for an assessment of the parameter range within which more simpler models based on assumptions like local thermal equilibrium or a sharp reaction front are valid.

REFERENCES

[1] VDI-Wärmeatlas, 2006.

[2] N. Böttcher, A.-K. Singh, O. Kolditz, and R. Liedl. Non-isothermal, compressible gas flow for the simulation of an enhanced gas recovery application. *Journal of Computational and Applied Mathematics*, 236(18):4933 – 4943, 2012.

[3] R. de Boer. *Trends in continuum mechanics of porous media*, volume 18. Kluwer Academic Pub, 2005.

[4] R. de Boer and A.K. Didwania. Saturated elastic porous solids: Incompressible, compressible and hybrid binary models. *Transport in Porous Media*, 45:423–443, 2001.

[5] W. Ehlers. Foundations of multiphasic and porous materials. In W. Ehlers and J. Bluhm, editors, *Porous Media: Theory, Experiments and Numerical Applications*, pages 4–86. Springer, Berlin, 2002.

[6] T. Graf. *Multiphasic flow processes in deformable porous media under consideration of fluid phase transitions*. PhD thesis, University of Stuttgart, 2008.

[7] O. Kolditz, S. Bauer, L. Bilke, N. Böttcher, J.O. Delfs, T. Fischer, U.J. Görke, T. Kalbacher, G. Kosakowski, C.I. McDermott, et al. Opengeosys: an open-source initiative for numerical simulation of thermo-hydro-mechanical/chemical (thm/c) processes in porous media. *Environmental Earth Sciences*, pages 1–11, 2012.

[8] B. Michel, N. Mazet, S. Mauran, D. Stitou, and J. Xu. Thermochemical process for seasonal storage of solar energy: Characterization and modeling of a high density reactive bed. *Energy*, (in press), 2012.

[9] T. Nagel, H. Shao, A.K. Singh, N. Watanabe, C. Roßkopf, M. Linder, A. Wörner, and O. Kolditz. Non-equilibrium thermochemical heat storage in porous media: Part 1 – conceptual model. *Energy*, submitted.

[10] T. Ricken and J. Bluhm. Modeling fluid saturated porous media under frost attack. *GAMM-Mitteilungen*, 33(1):40–56, 2010.

[11] F. Schaube, A. Wörner, and R. Tamme. High temperature thermochemical heat storage for concentrated solar power using gas–solid reactions. *Journal Solar Energy Engineering*, 133(3):031006, 2011.